Biomedical Microdevices (2020) 22: 42
https://doi.org/10.1007/s10544-020-00496-2

Effect of angle-of-attacks on deterministic lateral displacement (DLD) with symmetric airfoil pillars

Kawkab Ahasan[1] · **Christopher M. Landry**[1] · **Xiaolin Chen**[1] · **Jong-Hoon Kim**[1]

Abstract

Deterministic lateral displacement (DLD) is a microfluidic technique for size fractionation of particles/cells in continuous flow with a great potential for biological and clinical applications. Growing interest of DLD devices in enabling high-throughput operation for practical applications, such as circulating tumor cell (CTC) separation, necessitates employing higher flow rates, leading to operation at moderate to high Reynolds number (*Re*) regimes. Recently, it has been shown that symmetric airfoil shaped pillars with neutral angle-of-attack (AoA) can be used for high-throughput design of DLD devices due to their mitigation of vortex effects and preservation of flow symmetry under high Re conditions. While high-Re operation with symmetric airfoil shaped pillars has been established, the effect of AoAs on the DLD performance has not been investigated. In this paper, we have characterized the airfoil DLD device with various AoAs. The transport behavior of microparticles has been observed and analyzed with various AoAs in realistic high-Re. Furthermore, we have modeled the flow fields and anisotropy in a representative airfoil pillar array, for both positive and negative AoA configurations. Unlike the conventional DLD device, lateral displacement has been suppressed with +5° and + 15° AoA configurations regardless of particle sizes. On the other hand, stronger lateral displacement has been seen with −5° and − 15° AoAs. This can be attributed to growing flow anisotropy as *Re* climbs, and significant expansion or compression of streamlines between airfoils with AoAs. The findings in this study can be utilized for the design and optimization of airfoil DLD microfluidic devices with various AoAs.

Keywords Angle of attacks · High throughput · Deterministic lateral displacement · High Reynolds · Separation and purification · Symmetric airfoil

1 Introduction

Deterministic lateral displacement (DLD) is a microfluidic technique for size-based fractionation for particles/cells in continuous flow demonstrated by Huang et al. (Huang 2004). DLD devices consists of array of pillars, where each of the rows shift laterally compared to previous row. Due to inertial effects, when particles flow through the array, the particles having diameter smaller than a specific diameter, known as critical diameter (D_c) follow straight path, known as zigzag mode and the larger particles shift laterally, known as bumped mode. Early studies on DLD have focused on varying D_c with geometric parameters in laminar flow regimes, including the gap sizes (Zeming et al. 2016a) and various geometric pillar shapes (Zhang et al. 2015). In addition, external forces such as dielectrophoretic (Beech et al. 2009), gravitational (Devendra and Drazer 2012), and centrifugal forces (Jiang et al. 2016), and buffer additives such as sodium chloride (NaCl) (Zeming et al. 2016b) and Polyethylene glycol (PEG) (Chen et al. 2015), have been employed to improve the separation performance of DLD devices for a wide range of particle sizes. As a result, it has been extensively implemented to sort, concentrate, and isolate biological components, including circulating tumor cells (Loutherback et al. 2012; Okano et al. 2015), white blood cells (Civin et al. 2016), red blood cells (RBCs) (Beech et al. 2012), stem cells (Xavier et al. 2019), bacteria (Ranjan et al. 2014; Pariset et al. 2018), exosomes (Wunsch et al. 2016), and DNA (Chen et al. 2015; Wunsch et al. 2019).

Despite extensive research on DLD devices in the laminar flow regime, limited research has focused on the physics of flow, critical size of the device, and particle behavior in DLD

Electronic supplementary material The online version of this article (https://doi.org/10.1007/s10544-020-00496-2) contains supplementary material, which is available to authorized users.

✉ Jong-Hoon Kim
jh.kim@wsu.edu

[1] School of Engineering and Computer Science, Washington State University, Vancouver, WA 98686, USA

devices at moderate to high *Re* (Lubbersen et al. 2012; Dincau et al. 2018a). Furthermore, recent advances in biosensors have led to a strong demand for high-throughput sample preparation methods. With a growing interest in utilizing high-throughput DLD devices for practical applications, it has been demonstrated that symmetric airfoils with neutral angle-of-attack (AoA) can be used for high-throughput design of DLD devices due to their mitigation of vortex effects and preservation of flow symmetry under high *Re* conditions (Dincau et al. 2018b). Although high *Re* operation with symmetric airfoil shaped pillars has been established, there have been only a handful of studies on airfoil shaped pillar structures in DLD (Al-Fandi et al. 2011; Dincau et al. 2017). In aerodynamics, over decades of development, a wide variety of macroscale airfoils have been characterized for specific purposes, such as fuel efficiency, high-speed operation, and maximized payload. This has been achieved through careful selection of an airfoil's primary attributes – thickness, camber, and angle of attack – based on expected operating conditions (Abbott and Von Doenhoff 1959). Similarly, we hypothesized that airfoil arrays in DLD could also utilize those three attributes, in addition to array spacing, to optimize device performance for specific operations. In this paper, we have characterized the transport behavior of microparticles in DLD device via airfoil shaped pillars with various AoAs through numerical and experimental investigations. The AoAs for airfoil array are −5°, −15°, +5°, and + 15°. The flowrate is varied from 0.5 to 3.5 ml/min, and the corresponding *Re* ranges approximately from 1 to 40. We have also modeled the flow fields in a representative airfoil pillar array for both positive and negative AoA configurations and examined the anisotropy, which is the microfluidic array-induced lateral pressure gradient, leading to an inclined flow.

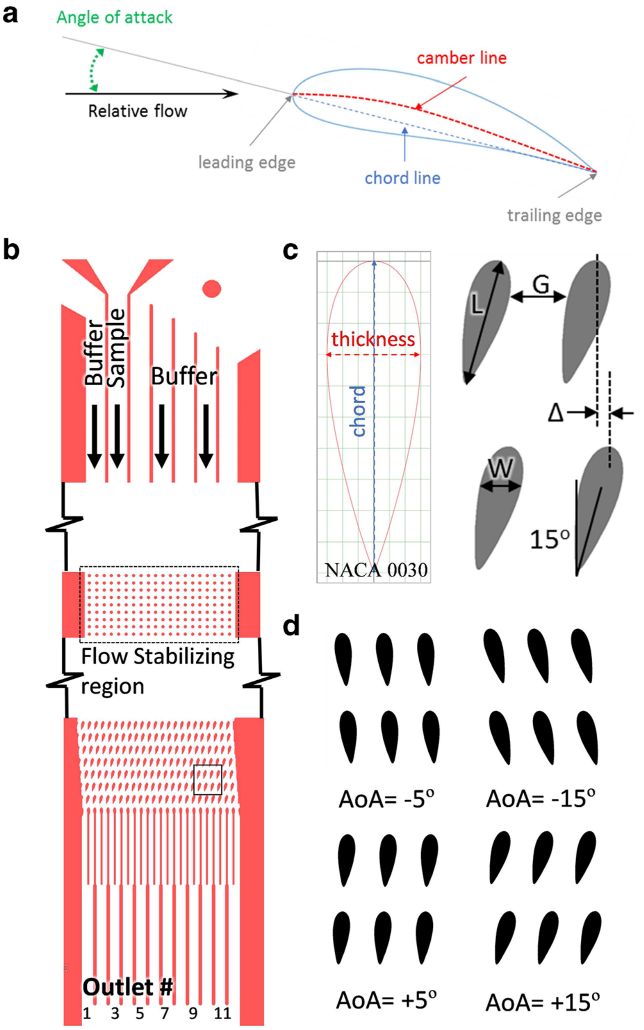

Fig. 1 **a** Airfoil nomenclature. **b** Airfoil DLD device design composed of array of airfoils, three inlets, filter sections, and flow stabilizing region. **c** A closer view of NACA 0030 airfoil and the +15° array, where length of the airfoil L = 90 μm, width of the airfoil W = 27 μm, lateral gap size G = 40 μm, and row shift Δ = 8.4 μm. **d** Four different AoA configurations showing rotation angle relative to the flow

2 Methodology

2.1 Airfoil device design and fabrication

The shape of the airfoil is defined using the geometrical parameters shown in Fig. 1a. The straight line drawn from the leading to trailing edges of the airfoil is called the chord line. The chord line cuts the airfoil into an upper surface and a lower surface. The camber line is a line drawn halfway between the upper and lower surface of airfoil. AoA is defined as the angle measured between the relative flow and chord line. The DLD device has array of airfoils, three inlets, filter sections, and flow stabilizing region as shown in Fig. 1b. The airfoil is designed based on NACA 0030. NACA 0030 is a symmetric airfoil where first 2 digit 00xx indicate that it has no camber and last 2 digit xx30 indicates that it has 30% thickness-to-cord ratio (Fig. 1c). Each airfoil has approximately 90 μm in length (L), 27 μm in thickness (W). The gap (G) size between airfoils is 40 μm and the row shift (Δ) is 8.4 μm.

The filter section is composed of 30 μm pillars with a gradual decrease of gap size from 50 μm to 35 μm in order to prevent any unwanted large sized particles from entering the main array. The flow stabilizing region is located between the inlet channels and the main array to reduce the secondary flow generation before the particle injection. The AoAs for an airfoil are −5°, −15°, +5°, and + 15° (Fig. 1d). The DLD devices are fabricated using traditional soft lithography techniques as described in our previous work (Dincau et al. 2018b). Briefly, a negative photoresist (SU-83050) is spin-coated and patterned on a 4-in. wafer, which is used to fabricate the DLD devices via polydimethylsiloxane (PDMS) casting. The PDMS device is then bonded to glass slide using oxygen plasma treatment. In order to reduce clogging problems, each device is treated with sodium dodecyl sulfate (SDS, 2 mM in DI water) for three hours.

2.2 Experimental study

The experimental setup uses a set of syringe pumps (kdScientific KDS-200, New Era NE-1000X, 1010) to drive the buffer and sample injection. The flowrate of each syringe pump is manually adjusted to achieve desired flow rate. The seed particles (2-μm) are injected to all the inlets to check the flow uniformity across the device. To study the effect of AoAs on DLD, three different size polystyrene particles (15-, 20-, and 25-μm) are used for each device. The particle trajectories are captured using high speed camera (Phantom Miro 310). The framerate is varied from 3000 to 10,000 frames per second based on the flow rate. For *Re* calculation, we use the following parameters with the properties of water: density $\rho = 1000\ \mathrm{m}^3/\mathrm{s}$, viscosity $\mu = 0.00089$ kg/m s (at 25 °C), and characteristic length L = 40-μm. Particle velocities are calculated using the phantom camera control (PCC) application, wherein individual particles are manually traced from frame-to-frame. Particle trajectories are obtained based on the particle distribution at the outlet, which is subdivided into 12 narrow outlets, illustrated in Fig. 1b. These outlets are numbered from left to right. The leftmost outlet is 1 and rightmost outlet is 12. Based on the outlet numbering scheme and device configuration, low numbered outlets (1–4) indicate a zigzag mode and high-numbered outlets (9–12) indicate a bumped mode. Particles in between outlets (5–8) are characterized as a mixed mode. Particles are manually counted as they passed through each outlet (1–12) by reviewing individual frames of the high-speed video. Since the precise number of particles varies between recordings, the curves are normalized for direct comparison.

2.3 Flow field and Array anisotropy study

Finite element-based software package, COMSOL Multiphysics is employed to model the 2D flow fields for several pillar orientations. To be consistent with experimental results, pillars are modeled as NACA0030 airfoils with various AoAs covering the entire range of experimental testing. The resulting airfoils have a maximum length of 90 μm and maximum thickness of 27 μm. Boundary conditions are set such that the inlet is governed by constant flow velocity, the outlet is fixed at atmospheric pressure, and remaining boundaries are set to the no-slip condition. Fluid properties are set to match those of water. To find the velocity flow fields, the Navier-Stokes and continuity equations are solved. From these solutions, streamlines are generated and plotted at prescribed locations that correspond to either stall lines or equal flux lines, which are used to visualize variations within the flow field amongst different AoA devices. Additionally, array anisotropy is evaluated by measuring the change in pressure across unit cell boundaries along the axial and lateral directions. Here array anisotropy is defined as a dimensionless ratio:

$$Anisotropy = \frac{\Delta P_{lat.}}{\Delta P_{ax.}}$$

where $\Delta P_{\mathrm{lat.}}$ is the lateral pressure drop and $\Delta P_{\mathrm{ax.}}$ is the axial pressure drop across a single unit of the array, see Fig. 2.

3 Results and discussion

To explore the effect of AoA, we have tested 4 different devices with different AoA of the symmetric airfoil pillars. Since we approximate the *Re* from various flow rates by directly measuring the particles velocities near the mid-array region, we check the linearity between volumetric flow rate and particle velocity in each device. These tests are performed by injecting a particle solution through all inlets of a device at a known flow rate set by the syringe pump, then determining the average particle velocity in the middle of the device using PCC software. A linear relation is obtained with R^2 near to 1, which confirms that our approximation is valid (See supplementary Fig. S.1). The uniformity of the flow across the channel is tested with 2-μm seed particles. The measured particle velocity at different location across the channel exhibits uniform trend (See supplementary Fig. S.2). The particle trajectories of 2-μm particles at multiple locations in the airfoil array are also observed (See supplementary Fig. S.3). The particles travel in a straight line, indicating uniform flow distribution across the channel.

3.1 Positive AoA devices

Figure 3 summarizes the experimental results for +5° AoA device with 15-, 20-, and 25-μm particles. Both 15- and 20-μm particles exhibit a pure zigzag mode and remain unchanged over the entire range of *Re* (Fig. 3a, b). However, the 25-μm particles show a zigzag mode up to *Re* = 26.4 and shift to mixed mode at *Re* = 36.6 (Fig. 3c). Figure 3d shows the summary of the particle distributions for +5° AoA with 15-,

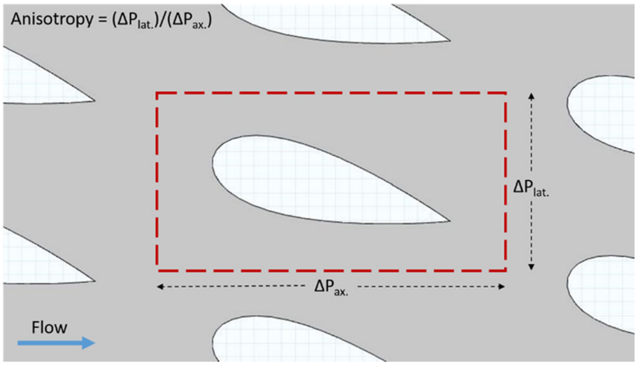

Fig. 2 Example of a repeating array unit used to determine values of anisotropy for different airfoil angles of attack, where ΔP is the pressure drop across the array unit

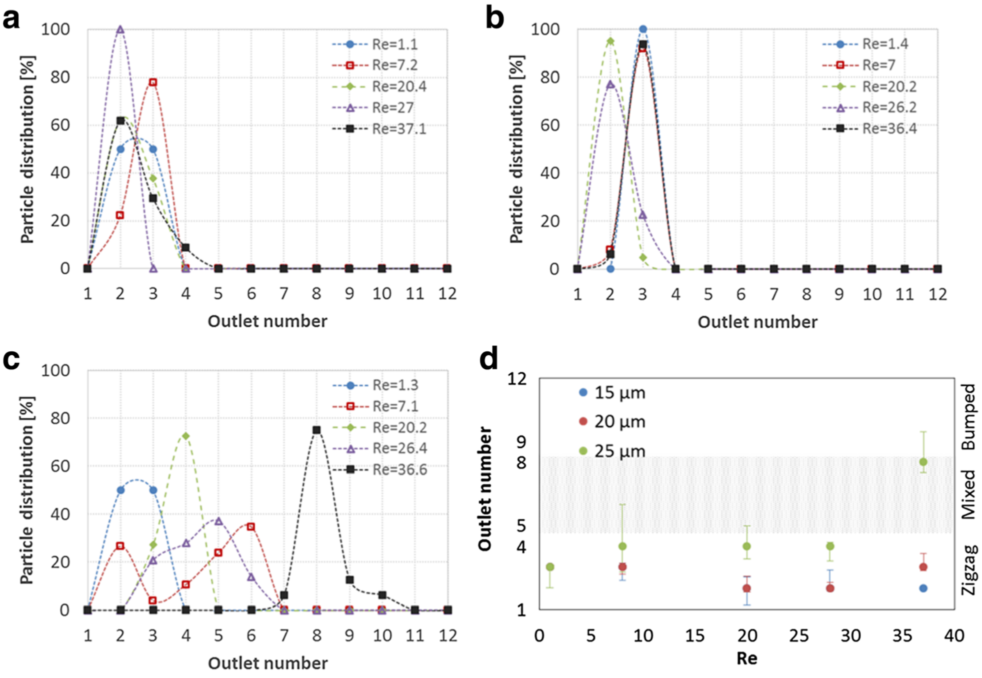

Fig. 3 Particle trajectory distributions of +5° AoA device with increasing *Re* for (**a**) 15-µm, (**b**) 20-µm, (**c**) 25-µm particles. (**d**) Summary of particle distributions at the outlets with increasing *Re*. Low numbered outlets (1–4) indicate a zigzag mode and high-numbered outlets (9–12) represent a bumped mode. Particles in between outlets (5–8) are characterized as a mixed mode. A zigzag mode is only observed for 15- and 20-µm particles. 25-µm particles follow a mixed mode at Re = 36.6

20-, and 25-µm particles. For this plot, we calculate a rounded up mean outlet number and standard deviation from each particle test at different *Re*. The rounded up mean outlet number represents the most likely path of injected particles and the standard deviation indicates their distribution at the outlet. We also take a rounded-up average of *Re* from each particle test for clear comparison, as the difference in *Re* between tests at the same flow rate is negligible. This plot indicates that the 15- and 20-µm particles show no shift in their outlet distribution, thus remain below D_c. However, the 25-µm particles demonstrate a particle trajectory transition from a zigzag to mixed mode at *Re* = 36.6.

Particle distributions at the outlet of +15° AoA device for 15-, 20-, and 25-µm particles are summarized in Fig. 4. With larger positive AoA device, all particles follow the zigzag mode over the entire range of *Re* regardless of their sizes as shown in Fig. 4a–c. The particles spread out within outlet #1–4 at low *Re*. However, their trajectories are even more shifted toward outlet #1–2 at high *Re* (Fig. 4a, b). This shift may be caused by strong flow anisotropy at higher flow rates (Dincau et al. 2018b). Figure 4d illustrates a summary of the results for +15° AoA device. This plot indicates that the D_c for +15° AoA device is always larger than 25-µm regardless of *Re*. Based on experimental observations, the particle trajectories with positive AoA differ from conventional DLD model in that the D_c becomes larger with increasing positive AoA.

To help elucidate the reason for the disparity, numerical simulation is employed for flow visualization with the extreme case of +15° AoA (Fig. 5). Note that we model a simplified device with a reduced period of $n = 3$ and display a small inset of the total model, representing a single period (See supplementary Fig. S.4). In this way, the flow field can be visualized with greater clarity and enhanced understanding of flow variation is achieved. Also, *Re* = 30 is chosen as representatively high *Re*. Figure 5a shows that stall lines in the positive device have undergone a change and no longer carry equal fluid flux as compared to the neutral device (See supplementary Fig. S.5). The stall lines for the positive device have undergone an expansion, displacing line 3 (blue) above line 1 (red). This effectively collapses a flow lane as the lane between 1 and 3 is too small for most particles to follow. Therefore, particles experience an effective reduction in total flow lanes. With the gap between pillars divided into fewer functional lanes, it is not likely for a particle to be large enough for its center to cross a stall line (bumped mode) without causing blockage. This observation can be seen by the large (yellow) particles of Fig. 5a that travel in a mixed mode.

Confirmation of this observed difference in particle behavior is established by looking at equal flux lines (Fig. 5b). For the positive AoA device, separating the flow between pillars into three equal fluid flux flow lanes shows that equal flux lines do not follow stall lines. From Fig. 5b, it is the second flow lane that splits around the successive row of pillars. This observation indicates that even a particle whose radius is larger than the first flow lane (conventionally the critical size) could move in a zigzag motion. If the radius is much larger than the width of the first flow lane, then it will likely cause blockage. Further inspection shows that even if the particle travels in the second flow lane and bumps over the second row, it would then be located in the third flow lane, which completely passes under the third row of pillars in a mixed motion. Lastly, streamlines in Fig. 5b do not return to their

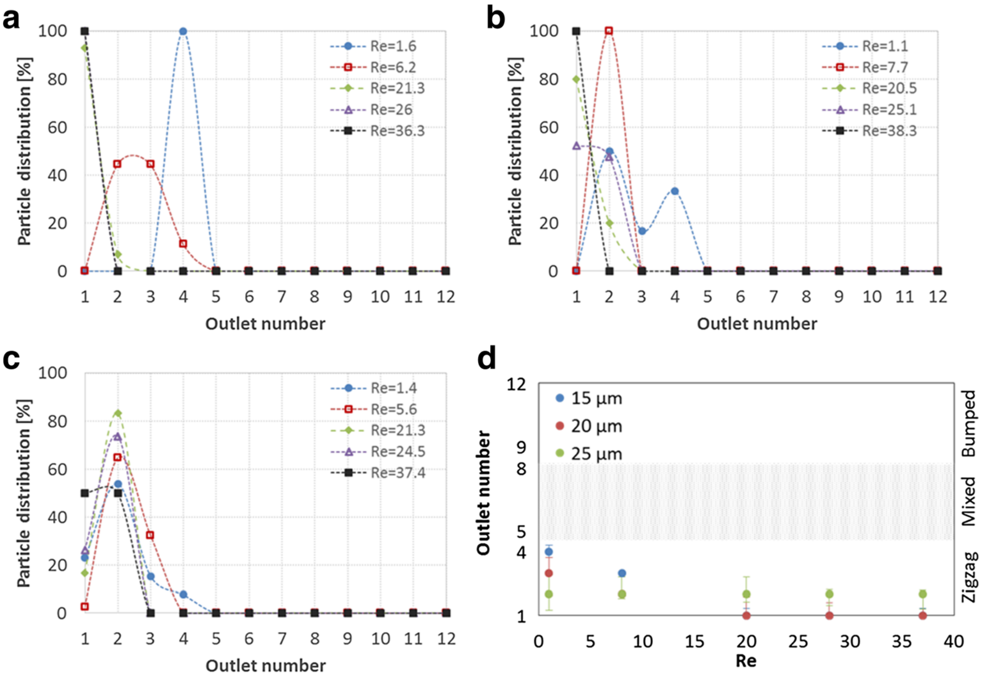

Fig. 4 Particle trajectory distributions in +15° AoA device with increasing *Re* for (**a**) 15-µm, (**b**) 20-µm, (**c**) 25-µm particles. (**d**) Summary of particle distributions at the outlets. All particles follow a zigzag mode and remain unchanged regardless of *Re*

relative gap position at the start of a new period. Rather they displace laterally downward, away from the direction of bumping. Therefore, it would be nearly impossible for any rigid particle small enough to prevent blockage issues to travel in a bumped mode through the device, which agrees well with experimental observation.

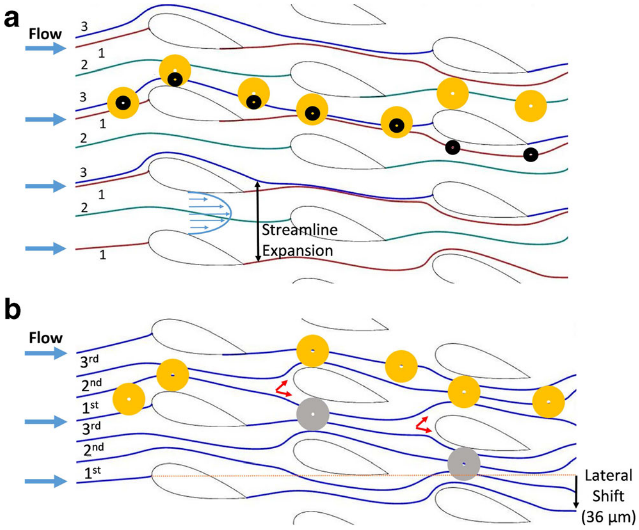

Fig. 5 Flow field diagram for symmetric airfoil device with a period of $n = 3$ and $Re = 30$. **a** Stall lines for +15° AoA device. Stall lines 1–3 demonstrate the expansion of flow lanes that no longer carry equal fluid flux. Both small (black) and large (yellow) particles travel in either zigzag or altered zigzag motion. **b** Equal flux lines for +15° AoA device with the lateral shift indicated as the vertical displacement from the streamline's point of origin (orange dashed line). The yellow particles represent the path of a particle following an altered zigzag mode, and the gray particles represent places where the particle could transition into zigzag mode

While the flow field analysis of positive devices strongly supports experimental observation, it does not explain why the flow field changed with AoA. Some current research suggests that array anisotropy, which is the microfluidic array-induced lateral pressure gradient, may be responsible for the change in flow field (Vernekar et al. 2017). Therefore, to help explain the change, array anisotropy is considered. From simulation, anisotropy of airfoil devices with positive AoA values are calculated for both low and high *Re* regime. For a summary of the anisotropy results, see Table 1. Here, the results from anisotropy analysis indicate a nearly perfect correlation between anisotropy and AoA, and that as *Re* increases so too does the magnitude of anisotropy. The positive value of anisotropy indicates a net force downward (zigzag direction) due to higher pressure on the top of the unit array than on the bottom. Because the flow fields are simulated at high *Re* regime, the corresponding downward force of anisotropy is more pronounced, thereby affecting the movement of fluid through the device. This causes the lateral shifting witnessed

Table 1 Anisotropy data for various AoA values at both high and low Re regime

AoA	Re = 0.51		Re = 30	
	Anisotropy (A)	$= \tan^{-1}A$	Anisotropy (A)	$= \tan^{-1}A$
0°	0.00	0.0°	0.00	0.0°
+5°	0.03	1.7°	0.10	5.7°
+15°	0.09	5.1°	0.29	16.2°
Correlation	1.0000	–	0.9999	–

in the streamlines for the +15° AoA device. Consequently, the effects of anisotropy are directly contributing to the increase in critical size of airfoil devices with positive AoAs at high *Re*.

3.2 Negative AoA devices

Figure 6 summarizes the particle distributions at the outlet of −5° AoA device with 15-, 20-, and 25-µm particles. The 15-µm particles exhibit zigzag mode with *Re* less than 10 (Fig. 6a). However, they show less drastic shift in their outlet distribution, whose peak remains at the mixed mode with increasing *Re*. Similarly, the 20-µm particles follow a zigzag mode up to *Re* = 7.5 and shift to the mixed mode as *Re* climbs (Fig. 6b). The 25-µm particles show the mixed mode across a range of *Re* values from 1.2 to 28.4 and shift to the bumped mode at *Re* = 37.8 (Fig. 6c). Figure 6d summarizes the particle distributions at the outlet for −5° AoA device. This plot shows that the D_c for −5° AoA device is in between 20- to 25-µm at low Re and D_c decreases with the increase of *Re*. The particles with −5° AoA device experience a clear, but less drastic shift with increasing *Re* when compared to −15° AoA device.

Figure 7 shows the particle distribution of 15-, 20-, and 25-µm particles for −15° AoA device. As shown in Fig. 7a, most of the 15-µm particles shows zigzag mode by following outlet #1–4 at low flow rates (*Re* = 1.5 and *Re* = 8.4). However, as the flow rate increases, the particles shift laterally to higher numbered outlets. At *Re* = 21.7, the particles are following a mixed mode, experiencing some lateral displacement, but following neither a pure zig-zag nor pure bumped trajectory. When *Re* = 28 and 37, the same particles follow a bumped mode. Similarly, the 20-µm particles also demonstrate a zigzag mode by following outlet #1–4 at *Re* = 1.4 (Fig. 7b). With the increase of flowrate, the particles start to follow a mixed mode at *Re* = 7.8. When *Re* = 19.3 and above, the particles follow a pure bumped mode. On the other hand, the 25-µm particles follow a bumped mode and remain unchanged over the entire range of *Re* (Fig. 7c). Figure 7d illustrates a summary of the results for −15° AoA device. This plot indicates that the D_c for −15° AoA device is in between 20- to 25-µm at low *Re* and it decreases with the increase of *Re* (Dincau et al. 2018a). Compared to the smaller negative AoA or positive AoA orientation, −15° AoA device yields a sharp transition from a zigzag mode to a bumped mode. The most likely contributor to this effect may be the array anisotropy that aligns with the lateral displacement direction in the negative AoA device.

As with the positive AoA devices, we observe that varying AoA can lead to a change in the particle trajectory. With negative AoA devices, the D_c is decreased with increasing AoA. Again, we employ numerical simulation to better understand the AoA effects. This time the flow field for the other extreme case of -15° AoA device is modeled (Fig. 8). The plotted stall lines for the -15° AoA device are shown in Fig. 8a. Opposite to the positive device, it can be seen that the stall lines for negative device have undergone significant compression, and no longer carry equal fluid flux. This compression of the stall lines makes it possible for a particle of smaller radius to cross streamlines and enter a higher flow lane. If the particle crosses to another flow lane, it is going to travel in either a mixed or bumped motion

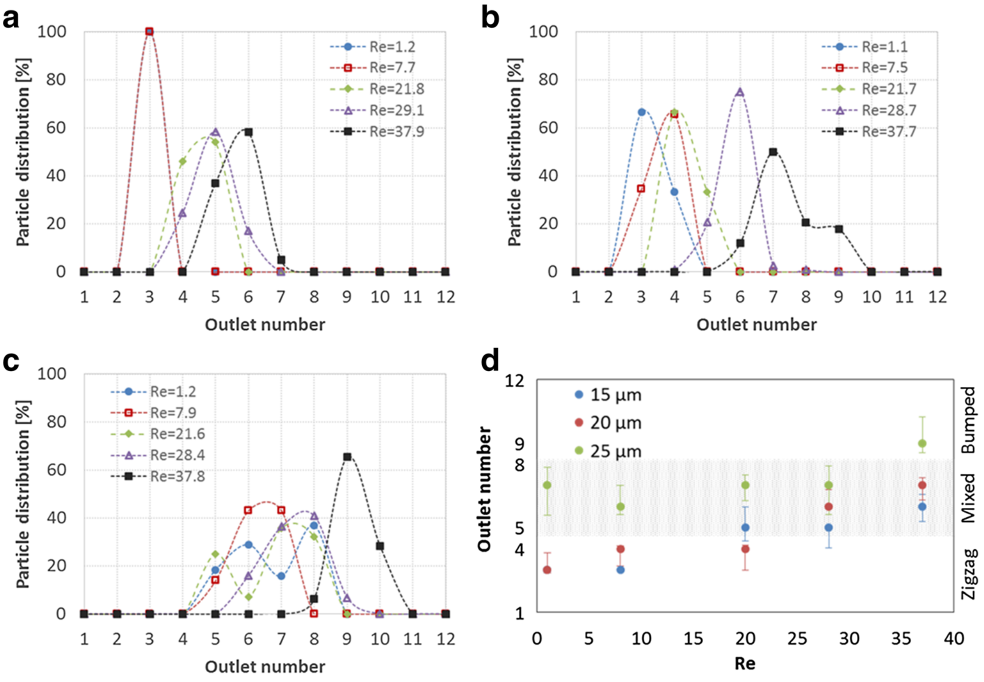

Fig. 6 Particle trajectory distributions in −5° AoA device with increasing *Re* for (**a**) 15-µm, (**b**) 20-µm, (**c**) 25-µm particles. (**d**) Summary of particle distributions at the outlets with increasing *Re*. The 15- and 20-µm particles only show zigzag and mixed modes over the entire range of *Re*. 25 µm particles follow a bumped mode at *Re* = 37

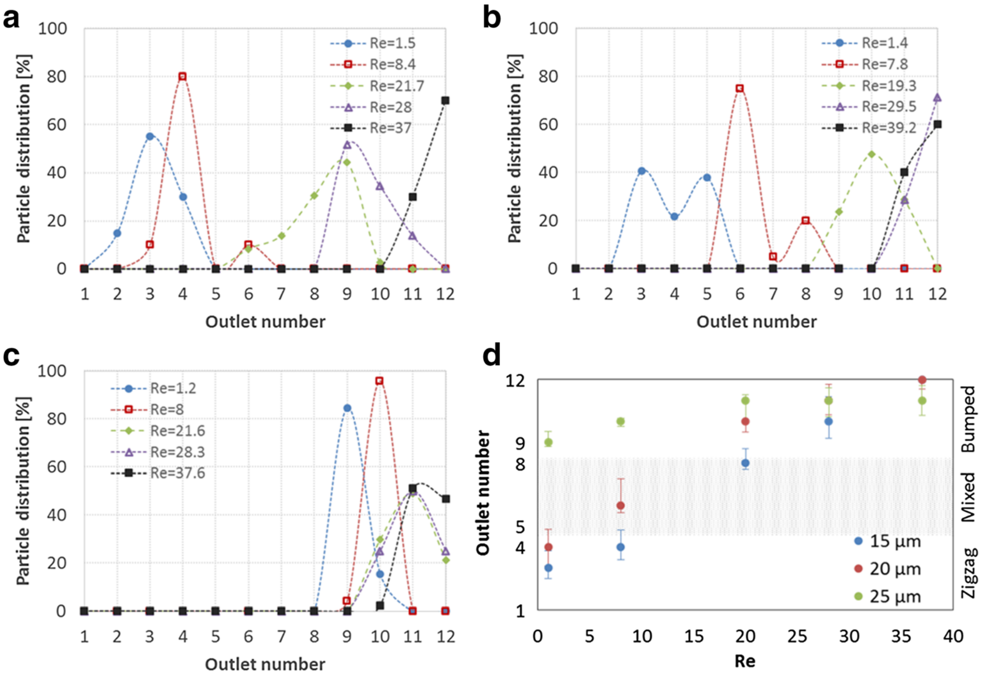

Fig. 7 Particle trajectory distributions in −15° AoA device with increasing *Re* for (**a**) 15-μm, (**b**) 20-μm, (**c**) 25-μm particles. (**d**) Summary of particle distributions at the outlets with increasing *Re*. A rounded up mean value of the outlet number was plotted with standard deviation. An average value is taken for determining the *Re*. A pure bumped mode is observed at $Re = 28$, $Re = 20$, and $Re = 1.2$ for 15-, 20-, and 25 μm particles, respectively

depending on whether it crossed one flow lane (black particle) or more flow lanes (yellow particle).

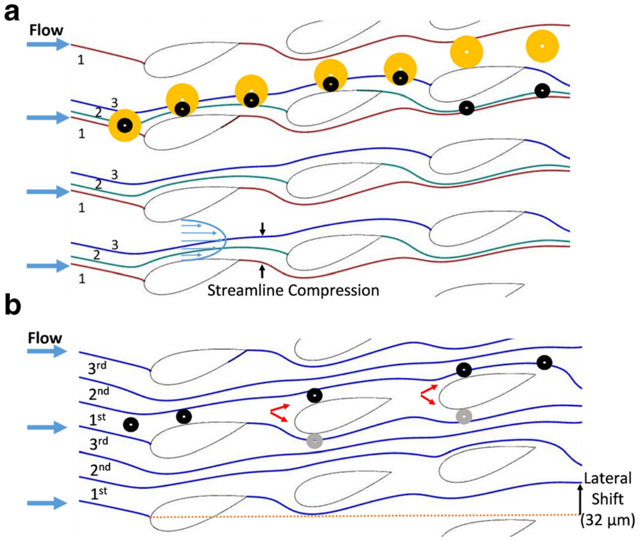

Fig. 8 Flow field diagram for symmetric airfoil device with a period of $n = 3$ and $Re = 30$. **a** Stall lines 1–3 show the compression of streamlines for -15° AoA device. Small (black) particles show the path of particles following altered zigzag motion (crossing only one stall line) and large (yellow) particles show the path of particles following bumped motion (crossing two stall lines). **b** Equal flux lines for -15° AoA device with the lateral shift indicated as the vertical distance from the streamline's point of origin (orange dashed line). The red arrows indicate splitting of a flow lane, leading to two potential paths. The black particles indicate the path of a particle small enough to fit within the first flow lane following bumped motion. The gray particles indicate places where the particle could transition from a bumped motion and enter an altered zigzag motion

To confirm the observed variation in particle behavior, equal flux lines are plotted for the negative device (Fig. 8b). Dividing the fluid flux through the gap between pillars into three equal flux flow lanes, as would be conventional for DLD devices, the flow lanes are not divided along stall lines as with the neutral device. Additionally, the next row of pillars does not bifurcate the first and second flow lanes as predicted by convention, but rather divides the first flow lane. A division of the first flow lane allows a particle trapped within this lane to potentially travel in either bumped mode or mixed mode, without leaving the current lane. Likewise, the third and last row in the period also divides the first flow lane, giving a particle small enough to fit within the first flow lane the opportunity to bump into the next flow lane or enter mixed mode. Lastly, streamlines will not return to their relative gap position by the start of the next period, but rather displace laterally upward in the direction of bumped mode. This confirms that smaller particles, even ones able to remain in the first flow lane, are likely to experience a lateral shift in the bumped direction leading to a mixed or bumped motion and agrees well with experimental observation.

To help explain why the flow field changed with angle of attack, array anisotropy is considered like the positive AoA. From simulation, anisotropy of airfoil devices with negative AoA values are calculated for both high and low *Re* regime. For a summary of the anisotropy results, see Table 2.

The results from anisotropy analysis indicate a strong correlation between anisotropy and AoA, and that as *Re* increases so too does the magnitude of anisotropy. Note that a negative value of anisotropy indicates pressure on the bottom of the

Table 2 Anisotropy data for various AoA values at both high and low Re regime

AoA	Re = 0.51		Re = 30	
	Anisotropy (A)	$= \tan^{-1}A$	Anisotropy (A)	$= \tan^{-1}A$
0°	0.00	0.0°	0.00	0.0°
-5°	−0.06	−3.4°	−0.10	−5.7°
-15°	−0.10	−5.7°	−0.26	−14.6°
Correlation	0.9538	–	0.9983	–

array unit is greater than pressure on the top, thereby creating a net force in the upward (bumped direction). Because the flow fields are simulated at high *Re* regime, the corresponding upward force of anisotropy is more pronounced, thereby affecting the movement of fluid through the device. This causes the lateral shifting witnessed in the streamlines for the – 15° AoA device. Consequently, the effects of anisotropy are directly contributing to the decrease in critical size of airfoil devices with negative AoAs at high *Re* number.

The relationship between AoA and particle trajectories with increasing *Re* is summarized in Fig. 9. In this graph, we have plotted the experimental results for each device with 20-μm particles as a function of *Re* and added a linear trend line for the comparison. The negative configuration yields a stronger shift with increasing AoA, while the positive configuration suppresses lateral displacement over most flow rates. This can be attributed to the significant expansion or compression of streamlines undergone between airfoils with AoAs. Furthermore, we note that local change in the critical separation result from the growing anisotropy with increasing *Re*. These results not only confirm the dependence of the D_c on *Re* in DLD device, but also elucidate the influence of AoA for airfoil shaped pillars on particle trajectories. Most notably that D_c varies with both AoA and *Re*, which should be accounted for in the initial design phases.

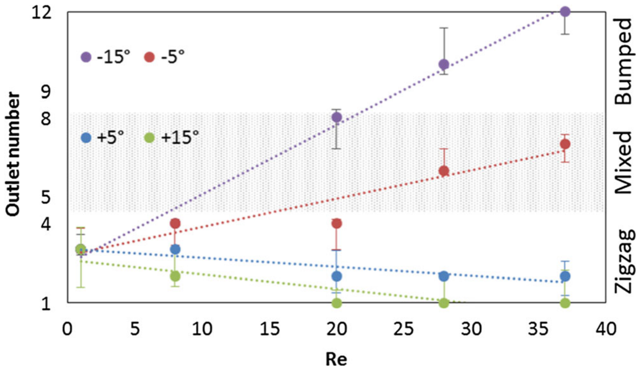

Fig. 9 Plot summarizing the experimental results with 20-μm particles to show the relationship between AoA and particle trajectories with increasing *Re*. The dashed line represents a linear fit for each AoA device. The positive configuration yields a zigzag mode regardless of *Re*, while the negative AoA configuration yields a sharp transition in particle trajectories with increasing *Re*

4 Conclusion

DLD holds a promise as a biosample preparation method for label-free and continuous passive size-based particle separation. Thus, various modifications from original DLD design have been made for enhanced performance in terms of separation resolution and throughput. High throughput operation requires high flow rates in DLD devices, resulting in operation under moderate to high *Re* regimes. Previously, it has been shown that symmetric airfoil shaped pillars with neutral AoA configuration hold off the vortex emergence in the wake of pillars as *Re* climbs, which can be used to improve separation resolution for high-throughput design of DLD devices. In this study, we have characterized the airfoil DLD device with various AoAs, both numerically and experimentally. We have demonstrated the transport behavior of microparticles in DLD devices with various AoA configurations. The lateral displacement has not been observed with +5° and + 15° AoA configurations regardless of particle sizes. On the other hand, a stronger lateral displacement has been seen with −5° and − 15° AoAs. The primary contributor for this change is that the stall lines for AoA devices have undergone significant variations with AoA, which make it possible for a particle to cross and enter a different flow lane compared to what it used to have in conventional DLD device. Furthermore, flow anisotropy is proportional to AoA. As *Re* increases, the corresponding upward or downward force of anisotropy are more pronounced, resulting in the movement of fluid through the device. Thus, anisotropy effects are directly contributing to the shift in critical size of airfoil devices depending on the AoA. The findings in this study can be utilized for the design and optimization of airfoil DLD microfluidic devices with various AoAs. Both AoA and *Re* should be accounted for in the initial design phases as D_c varies with both. Additionally, the large AoA may not be used for DLD design as it can significantly increase anisotropy as well as variations in streamlines, resulting in unpredictable particle trajectory and excessive fluid resistance. These are essential criteria if DLD is to be considered as a commercializable sample preparation technique, as throughput and resolution are the defining qualities of any purification device. It would be worthy of further investigation for different airfoil shapes to obtain a more comprehensive understanding of DLD mechanics.

Acknowledgements JK acknowledges partial financial support from the National Science Foundation (NSF CBET- 1707056). XC acknowledges partial financial support from the National Science Foundation (NSF ECCS- 1917299).

References

I. H. Abbott and A. E. Von Doenhoff, Theory of wing sections, including a summary of airfoil data, Corr. , ed. New York,: Dover Publications (1959)

M. Al-Fandi, M. Al-Rousan, M.A.K. Jaradat, L. Al-Ebbini, New Design for the Separation of microorganisms using microfluidic deterministic lateral displacement. Robot. Comput. Integr. Manuf. **27**(2), 237–244 (2011)

J.P. Beech, P. Jönsson, J.O. Tegenfeldt, Tipping the Balance of Deterministic Lateral Displacement Devices Using Dielectrophoresis. Lab Chip **9**(18), 2698 (2009)

J.P. Beech, S.H. Holm, K. Adolfsson, J.O. Tegenfeldt, Sorting Cells by Size, Shape and Deformability. Lab Chip **12**(6), 1048 (2012)

Y. Chen, E.S. Abrams, T.C. Boles, J.N. Pedersen, H. Flyvbjerg, R.H. Austin, J.C. Sturm, Concentrating Genomic Length DNA in a Microfabricated Array. Phys. Rev. Lett. **114**(19), 198303 (2015)

C.I. Civin, T. Ward, A.M. Skelley, K. Gandhi, Z. Peilun Lee, C.R. Dosier, J.L. D'Silva, Y. Chen, M. Kim, J. Moynihan, X. Chen, L. Aurich, S. Gulnik, G.C. Brittain, D.J. Recktenwald, R.H. Austin, J.C. Sturm, Automated leukocyte processing by microfluidic deterministic lateral displacement: Automated microfluidic blood leukocyte processing. Cytometry **89**(12), 1073–1083 (2016)

R. Devendra, G. Drazer, Gravity driven deterministic lateral displacement for particle separation in microfluidic devices. Anal. Chem. **84**(24), 10621–10627 (2012)

Dincau, B., Aghilinejad, A., Kim, J.-H., and Chen, X., Characterizing the High Reynolds Number Regime for Deterministic Lateral Displacement (DLD) Devices. *Volume 10: Micro- and Nano-Systems Engineering and Packaging*, ASME, Tampa, Florida, USA, p. V010T13A033 (2017)

B.M. Dincau, A. Aghilinejad, T. Hammersley, X. Chen, J.-H. Kim, Deterministic lateral displacement (DLD) in the high Reynolds number regime: High-throughput and dynamic separation characteristics. Microfluid. Nanofluid. **22**(6) (2018a)

B.M. Dincau, A. Aghilinejad, X. Chen, S.Y. Moon, J.-H. Kim, Vortex-Free High-Reynolds Deterministic Lateral Displacement (DLD) via Airfoil Pillars. Microfluid. Nanofluid. **22**(12), 137 (2018b)

L.R. Huang, Continuous particle separation through deterministic lateral displacement. Science **304**(5673), 987–990 (2004)

M. Jiang, A.D. Mazzeo, G. Drazer, Centrifuge-Based Deterministic Lateral Displacement Separation. Microfluid. Nanofluid. **20**(1), 17 (2016)

K. Loutherback, J. D'Silva, L. Liu, A. Wu, R.H. Austin, J.C. Sturm, Deterministic Separation of Cancer Cells from Blood at 10 ML/Min. AIP Adv. **2**(4), 042107 (2012)

Y.S. Lubbersen, M.A.I. Schutyser, R.M. Boom, Suspension separation with deterministic ratchets at moderate Reynolds numbers. Chem. Eng. Sci. **73**, 314–320 (2012)

H. Okano, T. Konishi, T. Suzuki, T. Suzuki, S. Ariyasu, S. Aoki, R. Abe, M. Hayase, Enrichment of Circulating Tumor Cells in Tumor-Bearing Mouse Blood by a Deterministic Lateral Displacement Microfluidic Device. Biomed. Microdevices **17**(3), 59 (2015)

E. Pariset, C. Parent, Y. Fouillet, B. François, N. Verplanck, F. Revol-Cavalier, A. Thuaire, V. Agache, Separation of biological particles in a modular platform of cascaded deterministic lateral displacement modules. Sci. Rep. **8**(1), 17762 (2018)

S. Ranjan, K.K. Zeming, R. Jureen, D. Fisher, Y. Zhang, DLD pillar shape Design for Efficient Separation of spherical and non-spherical bioparticles. Lab Chip **14**(21), 4250–4262 (2014)

R. Vernekar, T. Krüger, K. Loutherback, K. Morton, W.D. Inglis, Anisotropic permeability in deterministic lateral displacement arrays. Lab Chip **17**(19), 3318–3330 (2017)

B.H. Wunsch, J.T. Smith, S.M. Gifford, C. Wang, M. Brink, R.L. Bruce, R.H. Austin, G. Stolovitzky, Y. Astier, Nanoscale lateral displacement arrays for the separation of Exosomes and colloids down to 20 nm. Nat. Nanotech. **11**(11), 936–940 (2016)

B.H. Wunsch, S.-C. Kim, S.M. Gifford, Y. Astier, C. Wang, R.L. Bruce, J.V. Patel, E.A. Duch, S. Dawes, G. Stolovitzky, J.T. Smith, Gel-on-a-Chip: Continuous, velocity-dependent DNA separation using Nanoscale lateral displacement. Lab Chip **19**(9), 1567–1578 (2019)

M. Xavier, S.H. Holm, J.P. Beech, D. Spencer, J.O. Tegenfeldt, R.O.C. Oreffo, H. Morgan, Label-free enrichment of primary human skeletal progenitor cells using deterministic lateral displacement. Lab Chip **19**(3), 513–523 (2019)

K.K. Zeming, T. Salafi, C.-H. Chen, Y. Zhang, Asymmetrical deterministic lateral displacement gaps for dual functions of enhanced separation and throughput of red blood cells. Sci. Rep. **6**(1) (2016a)

K.K. Zeming, N.V. Thakor, Y. Zhang, C.-H. Chen, Real-time modulated nanoparticle separation with an ultra-large dynamic range. Lab Chip **16**(1), 75–85 (2016b)

Z. Zhang, E. Henry, G. Gompper, D.A. Fedosov, Behavior of Rigid and Deformable Particles in Deterministic Lateral Displacement Devices with Different Post Shapes. J. Chem. Phys. **143**(24), 243145 (2015)